Surface & Coatings Technology 494 (2024) 131354

Contents lists available at ScienceDirect

Surface & Coatings Technology

journal homepage: www.elsevier.com/locate/surfcoat

Surface hardening of high modulus steels through carburizing and nitriding: First insights into microstructure property relationships

M. Gathmann [a], N. Tönnißen [a], C. Baron [a], A. Kostka [b], M. Steinbacher [c], H. Springer [a,d,*]

[a] Max-Planck-Institut für Nachhaltige Materialien GmbH, Max-Planck-Strasse 1, 40237 Düsseldorf, Germany
[b] Ruhr-Universität Bochum, Zentrum für Grenzflächendominierte Höchstleistungswerkstoffe (ZGH), Universitätsstr. 150, 44780 Bochum, Germany
[c] Leibniz-Institut für Werkstofforientierte Technologien – IWT, Badgasteiner Str. 3, 28359 Bremen, Germany
[d] RWTH Aachen University, Metallische Verbundwerkstoffe, Intzestrasse 10, 52072 Aachen, Germany

ARTICLE INFO

Keywords:
Surface hardening
Lightweight design
High modulus steels
Particle transformation
Expanded ferrite

ABSTRACT

High modulus steels are promising materials for future lightweight design solutions, as their embedded boride particles in a ductile steel matrix increase the stiffness/density ratio. One key requirement for maturing them towards industrial application is their suitability for improving the surface hardness. In this study we investigated the effects of low-pressure carburizing and plasma nitriding on the microstructure and mechanical properties of selected Fe-TiB_2- and Fe-Cr-M_2B-based high modulus steels. Nitriding resulted with the formation of expanded ferrite in the strongest hardness increase to about 1100 HV0.05 from the alloy system's base hardness of 240 and 500 HV0.05, respectively, albeit with different hardness depth profiles. The Fe-Ti-B alloy indicated deformation phenomena in the ferritic matrix after nitriding, whereas nitriding of Fe-Cr-B-C resulted in a diffusion-controlled particle transformation of M_2B borides into CrN nitrides of lower stiffness. Carburizing on the other hand led to a slightly lower maximum hardness value of about 800 HV0.05 over an increased depth for Fe-Cr-B, as martensite and additional $M_{23}C_6$ carbides were formed in the surface zone. The surface hardness of the Fe-TiB_2-based alloy could not be increased by the deployed carburization parameters, most likely due to excessive Ti dissolved in the matrix. Consequences for the transfer to engineering applications as well as the refinement of both, thermo-chemical processing parameters and designated alloy concepts, of high modulus steels are outlined and discussed.

1. Introduction

Key factors for lightweight material design are an increased yield strength and materials' stiffness, expressed by the Young's modulus (E), as well as a reduced mass density (ρ) [1,2]. High modulus steels (HMS) as a type of metal-matrix-composites (MMC) designated for this purpose, combine stiff and low-density particles with a strong, ductile and cost-effective Fe-based matrix [3,4]. The most commonly researched HMS systems rely on 10–20 vol% of the very effective Titaniumdiborid (TiB_2; E of ~565 GPa; ρ of ~4.5 g cm^{-3} [5]) within a ferritic matrix, as it can be precipitated in-situ during liquid metallurgy synthesis [6–8]. By replacing titanium (Ti) with Chromium (Cr) as a boride forming element, M_2B-type particles are formed, which are slightly less effective than TiB_2 with regards to the E/ρ ratio [8,9]. However, Cr is usually cheaper than Ti, increases the stiffness of the matrix when kept in solid solution [10], reduces the tendency of floating and agglomeration during solidification [6,11] and allows the utilization of a Carbon (C)-containing steel matrix to adapt the property profile [9,12]. Particularly promising engineering applications for HMS are power transmitting components with tight geometric tolerances (and hence stiffness requirements) such as drive shafts, gearing bearings or gearings, but these parts generally require a surface hardness above the level of typical HMS materials.

From the multiple pathways to enhance the surface hardness of steels, carburizing and nitriding are the most widely established methods. Carburizing relies on enriching an austenitic surface layer with C to enable its subsequent transformation to hard martensite during cooling. Nitriding is performed at lower temperatures and aims to enrich the surface layer with Nitrogen (N). In this surface layer nitrides generally form a compound layer with a subjacent diffusion layer, where a hardness increase is achieved via precipitation of nitrides. Both processes are based on implementing interstitial elements, yet at different

* Corresponding author at: Max-Planck-Institut für Nachhaltige Materialien GmbH, Max-Planck-Strasse 1, 40237 Düsseldorf, Germany.
E-mail address: h.springer@mpie.de (H. Springer).

https://doi.org/10.1016/j.surfcoat.2024.131354
Received 24 May 2024; Received in revised form 6 September 2024; Accepted 9 September 2024
Available online 14 September 2024

temperatures and times, which in turn can be expected to interact with the diverse matrix and boride particles depending on the HMS alloy system. This study provides first insights into the underlying relationships between the hardening process, microstructure evolution and achievable properties in order to establish the basis for further alloy and process developments towards the successful production of surface hardened HMS components.

2. Material and methods

2.1. Sample production

The HMS base materials for the surface hardening investigations were Fe-7.2Ti-2.8B (Fe-7.15Ti-2.87B), Fe-6.0Cr-1.6B (Fe-6.01Cr-1.64B) and Fe-18.0Cr-1.6B-0.25C (Fe-18.0Cr-1.56B-0.273C). All chemical compositions are listed in wt% and the actual chemical compositions in the brackets were determined by wet chemical analysis. As the deviation between targeted and actual composition for all alloys was <0.1 wt%, the materials are specified by the nominal composition throughout this study. Syntheses of 800 g charges of the base material was performed by vacuum induction melting under Argon atmosphere followed by casting into a water-cooled copper-mold (25 × 60 mm). An exception was the Fe-18Cr-1.6B-0.25C base material which was casted into a Ø 20 mm copper-mold. The rectangular materials were hot rolled at 1150 °C to a thickness of 10 mm followed by air cooling. Swaging at 1150 °C with subsequently air cooling was performed on the Fe-18Cr-1.6B-0.25C material to generate a 15 mm diameter. The samples for the carburization and nitriding process were cut by spark erosion to the dimension of 25x30x8 mm and Ø 15 × 6 mm, respectively.

The Fe-Ti-B alloy was subjected to two thermochemical surface hardening techniques (plasma nitriding and low-pressure carburizing) investigated in this study. The Fe-Cr-B material was carburized only, while the Fe-Cr-B-C material was nitrided only. Both heat treatments aim at a surface close to the introduction of an interstitial to increase hardness, but do so in rather different ways. For carburizing, the specimens are fully austenitized and low-pressure carburized to introduce carbon. By quenching, the dissolved carbon in the surface layer will contribute to an increase in hardness mainly through the formation of carbon-rich martensite. By using the low-pressure carburizing technique, the often problematic surface oxide layer is less of a concern, as acetylene tends to reduce most of the thin oxide layer during the carburizing steps, and no reoxidation is likely to occur due to the low-pressure and oxide free atmosphere. Nitriding was performed using plasma nitriding to overcome the oxide layer, which can be a challenge for gaseous nitriding, especially for chromium-alloyed steels. The increase in hardness and strength obtained by nitriding is not due to martensitic transformation but to interstitial solution of nitrogen in the ferritic steel matrix and the formation of fine disperse precipitates such as γ'- or ε-nitrides along with alloy nitrides of chromium, titanium and boron. All three elements can contribute to hardness increase by forming alloy nitrides in the matrix. This is well known and understood for titanium and chromium, but there is little data in the literature for boron.

All samples were machined on all surfaces by hobbing and final face grinding. Before the samples were placed in the furnace, they were first washed in an aqueous medium at 70 °C for several minutes and then wiped with isopropanol.

Plasma nitriding was performed in an industrial hot wall plasma furnace of type Eltropuls H060x100 (batch volume Ø 400 × 900 mm, max. 1000 kg) at 540 °C. Along with the samples, an additional load (12 gear wheels) was added to the batch to simulate a higher load on the furnace. The heat treatment started with a convective heating step to 450 °C at 850 mbar in a N_2:H_2:Ar atmosphere (30 l/h, 3 l/h, 3 l/h) within 10 min. This was followed by a two-step sputtering at 500 °C and 530 °C for 30 min each at 600 V (PP 70:140 μsec) using the same atmosphere composition as the convective heating but at 1 mbar abs. Pressure. The purpose of the sputtering step was to remove any passivation layer and prepare the sample for nitrogen uptake during the subsequent nitriding step. After sputtering, the samples were heated to 540 °C and nitriding was started. The effective plasma nitriding was performed at 540 °C for 23 h in an atmosphere of 4 mbar and a N_2:H_2 ratio of 3:1 (50 l/h N_2 + 16.7 l/h H_2). The plasma parameters are PP 100:200 msec at ~500 V. The duration was kept low in order not to form a pronounced white layer on the sample surface, but to introduce enough nitrogen to achieve a penetration depth of 200–400 μm. Therefore, the nitrided samples should show a very shallow white layer and some diffusion and precipitation zone where nitrides could have formed. After the nitriding step, the samples were cooled in a furnace with active wall cooling under a nitrogen atmosphere.

Low-pressure carburizing was performed in a two-chamber vacuum furnace at 940 °C in a pulsed process using acetylene as carbon donor. The furnace used was an IPSEN RVFOQ with a charge size of 400x300x220 mm. Heating was performed at 30 K/min to 850 °C and 5 K/min to 940 °C. After 10 min of soaking, carburizing was started using alternating carburizing steps of a few minutes duration to increase the carbon content in the surface. The carburizing is carried out using 4 mbar of acetylene (200 l/h). During the vacuum phases without carburizing, an absolute pressure of about 5×10^{-2} mbar was applied.

The complete program in minutes (carb.diff..carb.diff..etc.) 1.20.0.1.20.0.1.5.30.0.1.5.40.0.1.5.60.0.1.5.90.0.1.5.100. The applied carburizing program aimed for a carburizing depth of about 1 mm for a mild carburizing steel grade (e.g. 20MnCr5). At the end of the carburizing, after a final diffusion step of 100 min, the batch was cooled to 850 °C in 20 min and soaked for another 20 min. The batch was then transferred to the quenching chamber under a nitrogen atmosphere and immersed in agitated vacuum oil at 60 °C. After washing the samples in a hot aqueous bath at 70 °C for 15 min, the samples were tempered at 180 °C for 2 h in a circulating air furnace.

2.2. Characterization

For microstructure analyses the cross-sectional areas of the hardened surfaces were prepared by grinding and polishing with standard metallographic techniques. Prior to the characterization with a light optical microscope (OM; Leica DM 4000 M) the samples were etched with 1 % Nital (100 ml ethanol and 1 ml nitric acid 65 % [13]). The Fe-18Cr-1.6B-0.25C material was etched with a V2A-etchant (100 ml distilled water, 100 ml hydrochloric acid 32 %, 10 ml nitric acid 65 % and 0.3 ml Vogels inhibiter [13]) at 60 °C. For further imaging of the etched, samples scanning electron microscopy (SEM, Jeol JSM-7200F) was performed and energy dispersive X-ray spectroscopy (EDS, Oxford AZtecEnergy X-MaxN 80 mm^2) was used to analyze the local chemical composition. Transmission electron microscopy (TEM; Jeol JEM-2100) was performed at selected locations in the surface layers and bulk materials, and was prepared with a focused ion beam system (FIB; FEI Helios G4 CX). Final milling of the tip was executed with low ion energies of 5 kV to minimize beam damage. TEM chemical analyses were performed using an Oxford Aztec Energy TEM Advanced X-MaxN 80 T EDS spectrometer. A Leco Microhardness tester LM 100 AT was used to determine the Vickers microhardness of the sample's cross-section. Each value of the displayed hardness profiles is the average of five indentations at the same distance to the surface with the corresponding standard deviation. From the hardness profiles, the hardness gradient was determined by the slope of the linear regression between the nearest indentation to the surface and the first indentation of the bulk material. The linear regressions are displayed by the dotted line in Fig. 1 a). For the nanoindentation analysis a TriboIndenter from Hysitron was used with a Ti 39–01 Bercovich indenter and 1000 μN. Scanning probe microscopy with a load of 2 μN in an area of 10 × 10 μm was used during nanoindentation to separate the different phases.

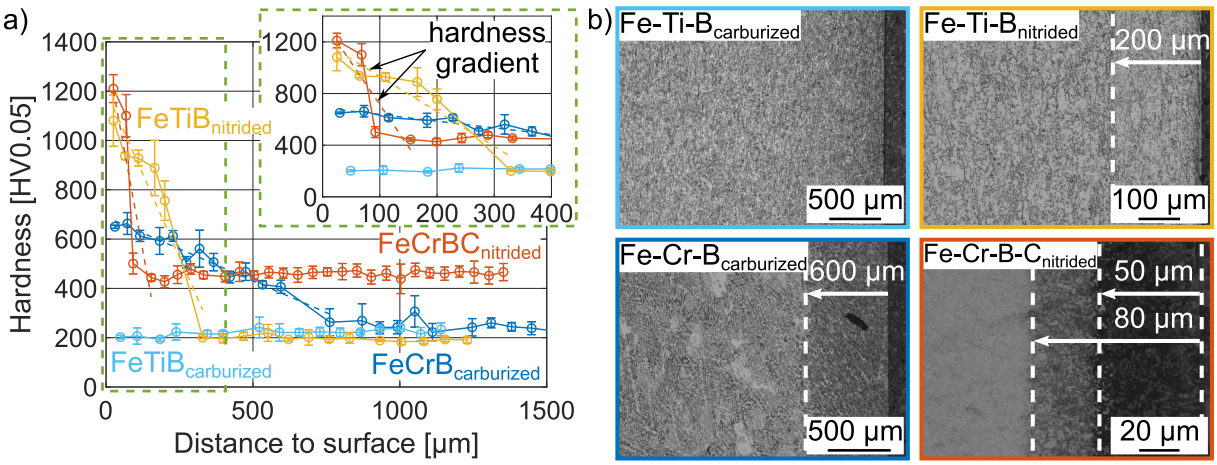

Fig. 1. Overview of various surface hardened Fe-TiB_2- and Fe-M_2B-based high modulus steels by carburizing and plasma nitriding a) hardness profile and hardness gradient (dotted line) b) optical micrographs along the cross section.

3. Results

An overview of the hardness profiles and OM images of the different HMS materials after surface hardening is provided by Fig. 1. All samples exhibited a similar hardness (~ 200 HV0.05) within the bulk material, with the exception of Fe-18Cr-1.6B-0.25C, whose carbide-containing matrix effectively doubles the bulk material hardness to ~470 HV0.05. No change within the treated surface area was observed for the carburized Fe-7.2Ti-2.8B material regarding both hardness values and microstructure. Low-pressure carburizing of Fe-6Cr-1.6B on the other hand resulted in an increased surface hardness with the thickest surface layer and lowest hardness gradient of −0.52 HV μm^{-1} – rendering in the smoothest hardness transition from the surface to the bulk material. In comparison to the carburizing process, both plasma nitrided samples show an even harder surface layer with a similar hardness peak close to the surface. Nitriding resulted in a significant smaller layer thickness with a more than twice as thick layer for the Fe-Ti-B alloy. The higher hardness gradients of nitrided Fe-Ti-B (−2.70 HV μm^{-1}) and Fe-Cr-B-C (−6.49 HV μm^{-1}) characterized the more sudden hardness drop, with a linear hardness decrease for Fe-Cr-B-C and a small hardness plateau for Fe-Ti-B. For the nitrided Fe-Cr-B-C the two zones, displayed by the different contrast in the OM image (Fig. 1 b)), could not be differentiated by the hardness profile due to the deployed resolution of the indentation step size.

3.1. Low-pressure carburizing

The SEM images in Fig. 2 of carburized Fe-7.2Ti-2.8B show a ferritic matrix (light grey) with embedded TiB_2 particles (dark grey). Both primary and eutectic particles are present due to the hypereutectic

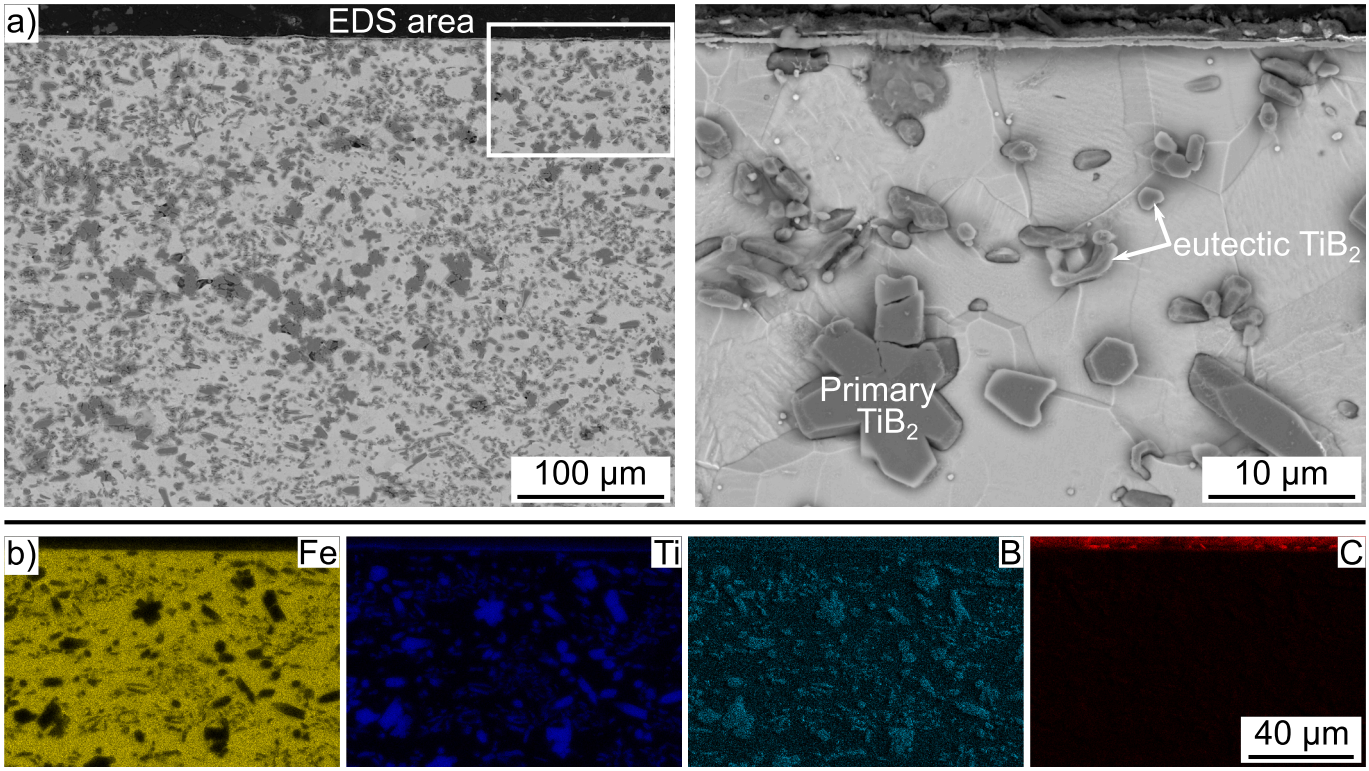

Fig. 2. Analyses of carburized Fe-7.2Ti-2.8B (wt%) a) SEM images of carburized surface area b) EDS maps for selected elements.

composition, with the primary TiB_2 particles being larger (diameter of about 10 μm) and clustered together as an effect of density induced agglomeration [6]. The EDS maps for specific elements in Fig. 2 b) display a qualitative view of the elemental distribution that highlights TiB_2 in the Ti- and B-map, while appearing black in the Fe-map. C was not detected inside the surface zone – the visible C-rich fringe was caused by the conductive embedding material. These results indicate that the carburization treatment of Fe-Ti-B did not lead to the desired uptake of C and hardness increase in the surface zone.

Carburization of Fe-6Cr-1.6B, however produced a 600 μm thick surface layer (Fig. 1) with a martensitic matrix (light grey) and M_2B particles (dark grey) as shown in Fig. 3 a). The M_2B inside the surface layer and the ferritic bulk material, which is displayed in Fig. 3 b), did not indicate major deviations regarding particle size or morphology. TEM analyses, displayed by a bright field (BF) micrograph and selected area diffraction patterns (SAD) about 20 μm distant to the surface reveal an α-Fe matrix and additional $M_{23}C_6$ carbides to the M_2B particles.

3.2. Plasma nitriding

The 200 μm section of the plasma nitrided Fe-7.2Ti-2.8B surface layer with TiB_2 particles (dark grey) and ferritic matrix (light grey) as well as an EDS map of N are shown in Fig. 4 a). The higher magnification of the surface area reveals a roughly 4 μm thick presumable compound layer, which seemed to be less affected by the etching process than the material underneath. This compound layer shows a higher N-content compared to the diffusion layer beneath. The matrix grains directly below the compound layer indicate a different morphology compared to the polygonal grains further distant to the surface layer and disclose fine bright lines after etching (exemplary marked by orange circle). Similar to the carburized Fe-Ti-B (Fig. 2 a)) the nitrided material shows black areas around big primary and clustered particles. The smaller eutectic TiB_2 particles in the diffusion layer indicate brighter spots inside the particles (displayed by arrows). A detailed investigation of an eutectic TiB_2 particle with brighter spots and the surrounding Fe matrix by qualitative EDS mapping, displayed in Fig. 4 b), shows accumulated iron and nitrogen inside the TiB_2. The indicated N-content in this particle is ascribed to the overlapping peaks of B and N, since a quantitative EDS analysis did not detect N inside the TiB_2 (not shown here). TEM analysis of Fig. 4 c) validates the matrix as α-Fe and the particles as TiB_2. The hardness and reduced Young's modulus (E_r) of the identified phases and zones were determined via nanoindentation and the indentation locations are schematically displayed by color coded circles in Fig. 4 a). Fig. 4 d) displays a superior hardness and E_r for TiB_2 compared to the different analyzed zones. The small compound layer, which could not be captured by the hardness profile of Fig. 1 a) due to its size, indicates a slightly lower hardness than the diffusion layer below.

Fig. 5 a) displays SEM images of the surface zone from the plasma nitrided Fe-18Cr-1.6B-0.25C. The 50 μm thick layer with a darker contrast displayed in the OM images (Fig. 1 b)) is also indicated here, however the zone with brighter contrast between 50 μm and 80 μm distance to the surface cannot be identified. EDS mapping in the surface zone only detected N for a roughly 50 μm thick layer. The particles in Fig. 5 b) indicate a transition from a bright to dark contrast, which resulted from the uptake of N and corresponding particle transformation. This transformation was a diffusion-controlled decomposition, as particles closer to the surface show a complete transformation. The uptake of N inside the surface zone resulted in cracks inside former M_2B particles and the surrounding matrix, which are indicated by arrows in the SEM image of Fig. 5 b). A total of three phases can be detected by TEM analysis. The matrix consists of α-Fe and the particles of Cr_2B. Poly-crystalline CrN was detected at the matrix/particle interface

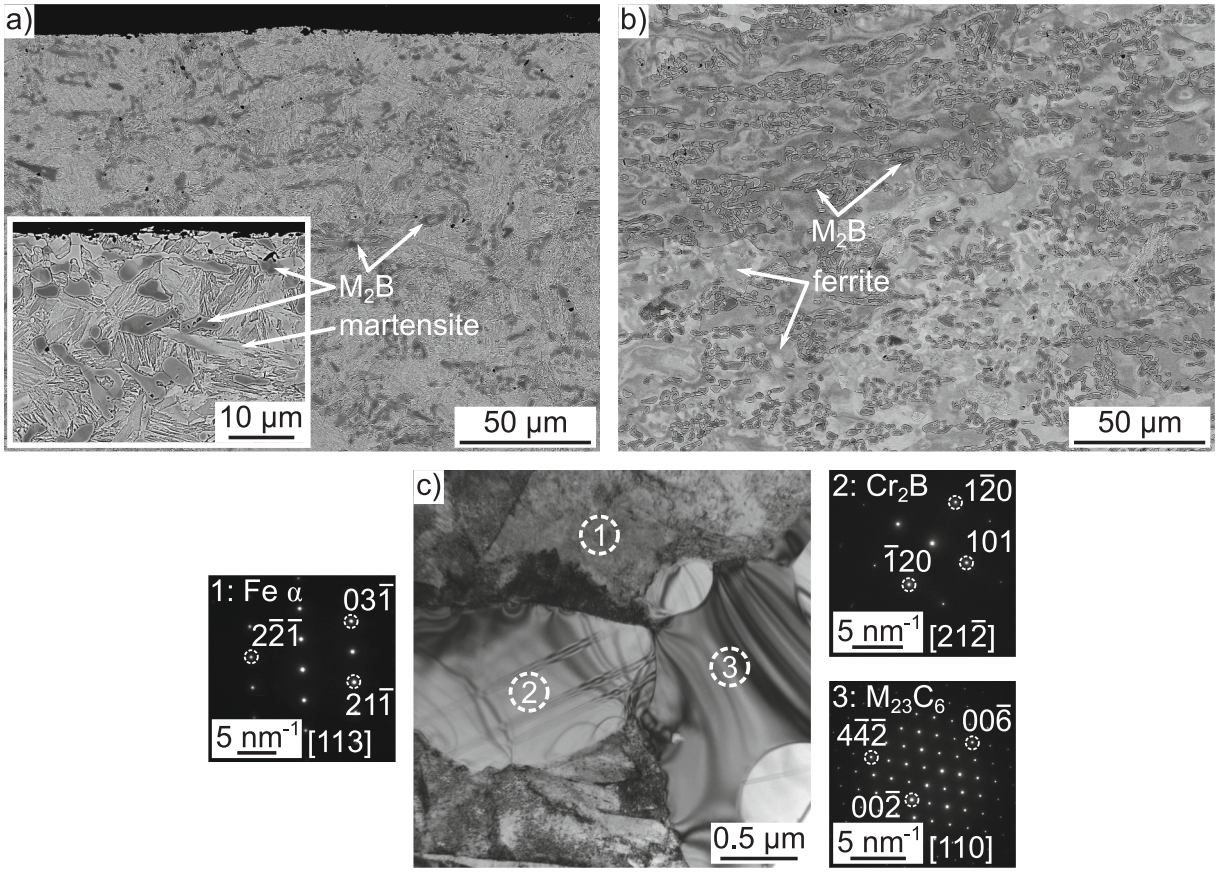

Fig. 3. Analyses of carburized Fe-6Cr-1.6B (wt%) a) SEM image of carburized surface area b) SEM image of bulk material c) TEM BF micrograph of surface area with corresponding SAD patterns.

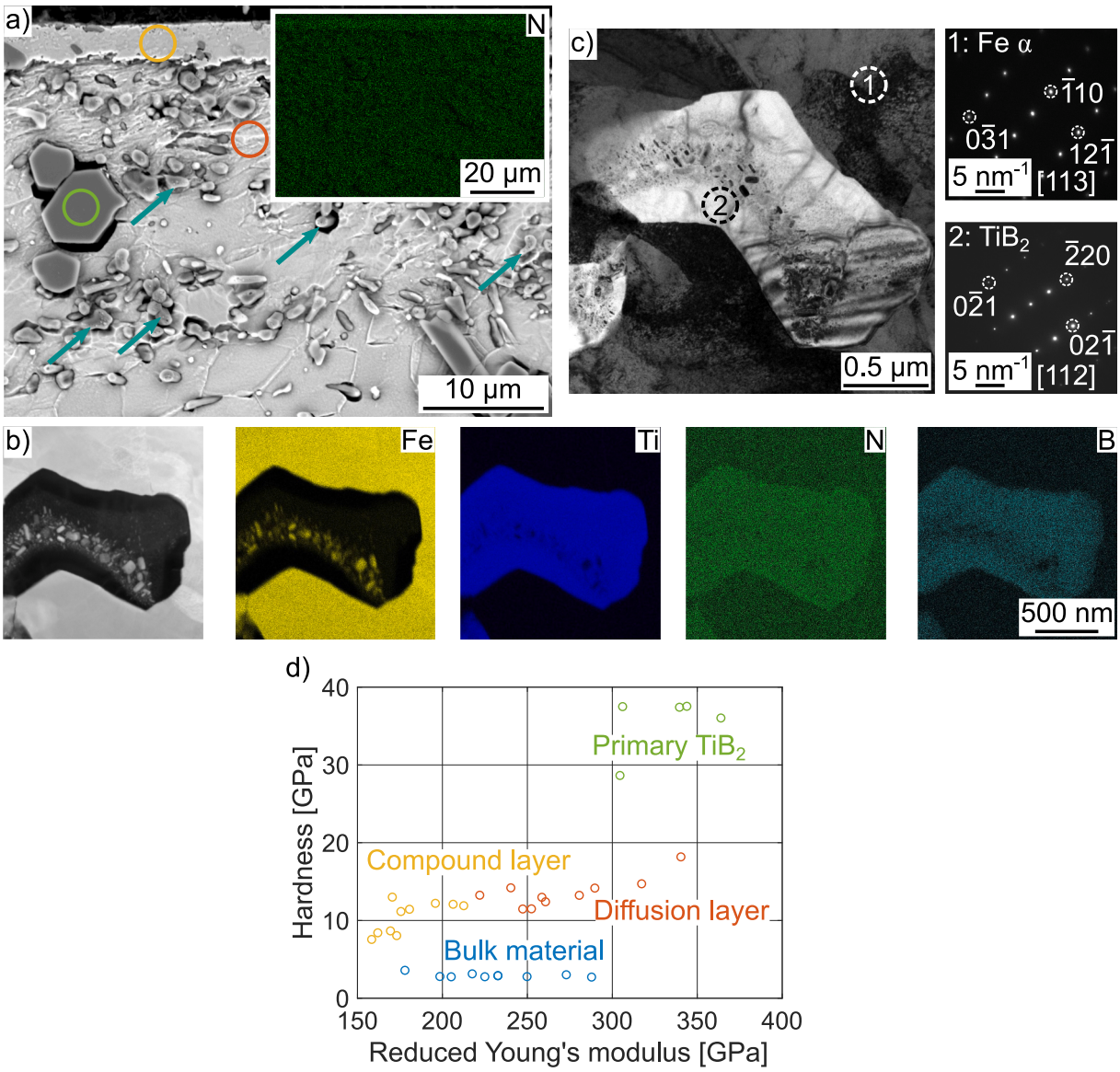

Fig. 4. Analyses of plasma nitrided Fe-7.2Ti-2.8B (wt%) a) SEM images of nitrided surface area with EDS mapping of N b) HAADF image and EDS maps for selected elements of nitrided surface area c) TEM BF micrograph of surface area with corresponding SAD patterns d) hardness and reduced Young's modulus for TiB_2 and different zones in nitrided surface area (investigated zones schematically marked in a)).

of a partly transformed particle. Hardness and E_r values for M_2B, CrN as well as the bulk material, measured at the schematically indicated locations in Fig. 5 b), are displayed in Fig. 5 d). The transformation of M_2B to CrN resulted in a distinct hardness and E_r decrease for the particles.

4. Discussion

4.1. Low-pressure carburizing

The carburization treatment of Fe-7.2Ti-2.8B did not result in the desired uptake of C (Fig. 2 b)) and hardness increase in the surface zone (Fig. 1 a)) like demonstrated for pure iron without ceramic particles [14,15]. One possible reason could be that the deployed furnace temperature of 940 °C was not sufficient to ensure austenitization of the sample, which limited the solution of C within the surface zone. There was no evidence of significant C diffusion into the material, and particles both close to as well as far away from the surface did not show changes in type (e.g. transformation of TiB_2 to TiC), size or morphology induced by the thermochemical treatment apart from known slight spheroidisation due to the heat treatment [16]. In Fe-Ti-B systems the Ti-content exceeds the required stoichiometric amount for TiB_2 to suppress the formation of Fe-borides and possible Ti-carbide, as there is almost no C in the matrix [7]. This excessive Ti-content in the matrix, which was not used for the TiB_2 formation, was quantified by TEM EDS between 1.18 and 1.67 at.% for the nitrided Fe-Ti-B alloy (chapter 4.2). Thereby, the excessive Ti in the matrix likely increased the austenite starting temperature, as the binary Fe—Ti system indicates a temperature increase up to a maximum Ti solubility in austenite at roughly 0.8 at.% and 1120 °C [17], which exceeded the employed carburization temperature (940 °C). Hence, the carburization of the Fe-Ti-B system was restricted by the excessive matrix' Ti-content, as it affected the required austenite formation.

In contrast to Fe-Ti-B, carburization of Fe-6Cr-1.6B accomplished the desired hardness increase in the surface zone. The austenite start temperature of roughly 846 °C, estimated by the binary Fe—Cr system [17], was exceeded by the process temperature (940 °C). Thus, carburizing generated austenite and resulted correspondingly in martensite formation that accomplished the evident hardness increase in the surface zone.

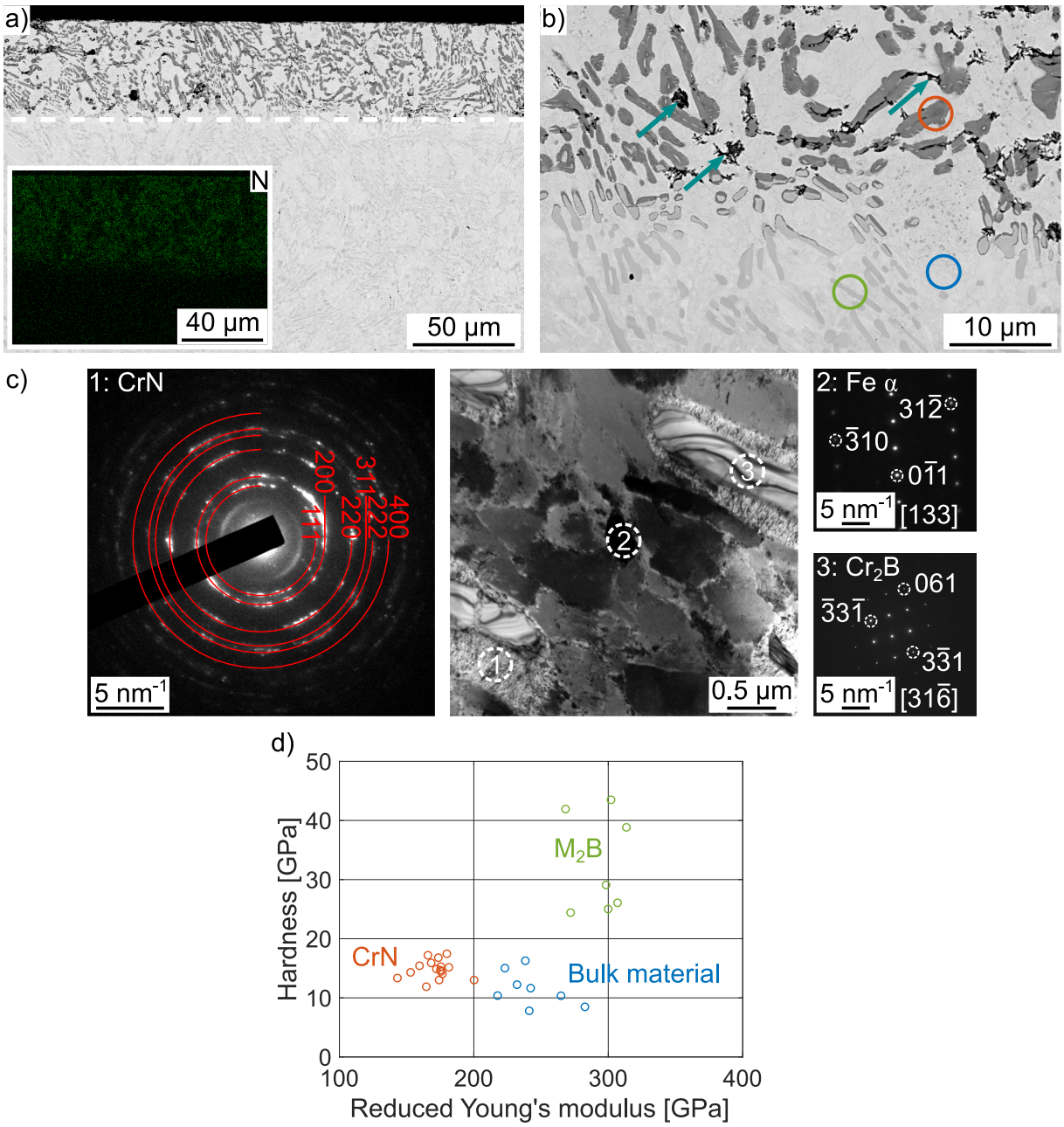

Fig. 5. Analyses of plasma nitrided Fe-18Cr-1.6B-0.25C (wt%) a) SEM image of nitrided surface with EDS mapping of N b) SEM image of transition zone c) TEM BF micrograph of surface area with corresponding SAD patterns d) hardness and reduced Young's modulus for different zones in the surface layer (investigated areas schematically marked in b)).

The employed analyzing methods did not reveal noticeable changes of the M_2B's structure or morphology during carburizing, however future investigations at even higher resolution (APT) are required to provide more detailed information. Carburizing of ferritic or martensitic stainless steels serve as a first classification of the surface hardened Fe-Cr-B, but should be carefully interpreted due to different mechanisms based on process parameter deviations. The achieved hardness exceeds the surface hardness of a low-temperature plasma carburized X12Cr13 martensitic stainless steel, which actually showed a small hardness decrease in the surface layer [18]. Compared to the nitriding treatments, the carburized Fe-6Cr-1.6B resulted in the smallest hardness gradient (-0.52 HV µm^{-1}), which diminishes the risk of premature damage due to cracks or spalling inside the hardened surface layer or transition zone.

4.2. Plasma nitriding

By plasma nitriding, the hardness of Fe-Ti-B was successfully increased to reach values >1000 HV0.05, yielding in a hardness nearly twice as high compared to nitrided pure iron [19]. Surface hardness enhancement by nitriding generally requires γ' (Fe_4N) and/or ε ($Fe_{2-3}N$) precipitations, which were not detected by performed SEM or TEM analyses [20]. However, the TEM analyses at the nitrided near-surface region revealed significantly diffused electron diffraction spots, which were further investigated with SAD patterns from a 200 nm diameter region. Samples of bulk and near-surface region were orientated to the zone axis [113]. Fig. 6 (b, f, c, g) display the selected enlarged diffraction spots (−211) and corresponding intensity profiles. The half-height peak width was used to characterize the Fe α crystallographic lattice distortion and was almost twice as wide at the near-

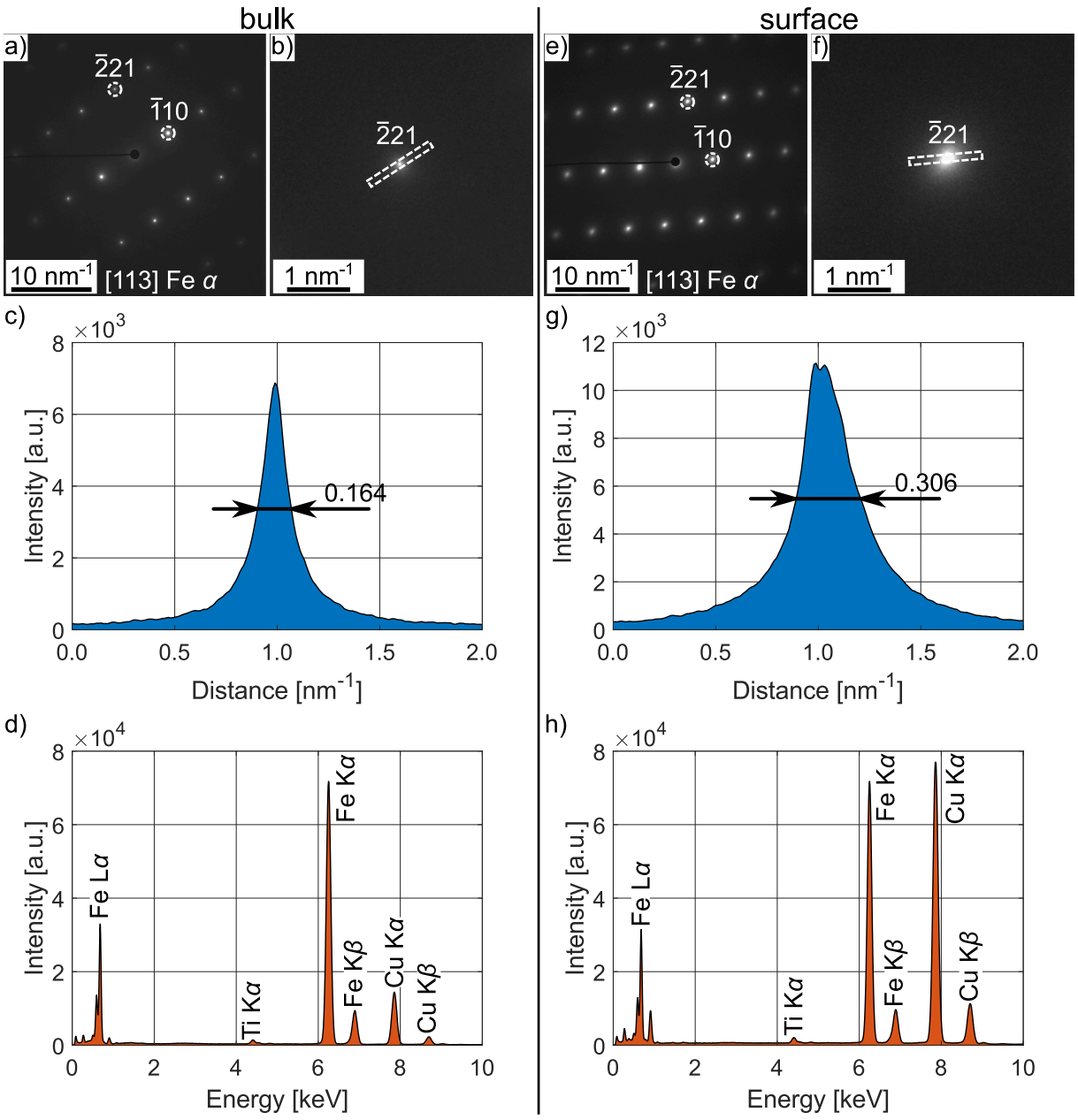

Fig. 6. TEM analyses of the plasma nitrided Fe-7.2Ti-2.8B (wt%) with SAD pattern oriented to the zone axis [113] (a, e), enlarged diffraction spot (b, f) with intensity profile of (−221) diffraction spot (c, g) and qualitive EDS spectrum acquired with a lifetime of 180 s each.

surface region, which was likely caused by dissolved atoms. Acquisition of EDS data at the same location and crystallographic orientation are shown in Fig. 6 (d, h). As the TEM lamella was mounted on a copper carrier the spectrum showed Cu peaks, which was higher for the near-surface sample due to the geometrical arrangement between the microscope (e-beam – two EDS detectors) and lamella. The number of counts of the Kα peaks in the EDS spectrum were similar for both measured regions, which references a similar TEM sample thickness. Comparison of quantified EDS data for dissolved elements in the near-surface (Ti = 1.67 at.%; N = 1.52 at.%) and bulk region (Ti = 1.18 at.%; N = 0.49 at.%) yielded in a three times higher N- as well as higher Ti-content for the nitrided surface area. Thus, the larger size of the diffracted spots on the SAD pattern of the near-surface region (Fig. 6 (e)) represents dissolved N and Ti atoms. Dissolved N in the form of expanded austenite (S-Phase) in austenitic stainless steels [21–23] and expanded ferrite α_N in ferritic stainless steel [24–26] yield in an increased surface hardness without relying on nitride precipitation. Expanded ferrite most likely led to the surface hardness increase after nitriding, as the higher lattice distortion due to dissolved N indicates the formation of α_N and no nitrides were detected in the surface zone. Future in-depth analyses with XRD or APT are required to confirm the solely presence of expanded ferrite and its effect on the surface hardness increase for HMS. Fe-rich precipitations were only detected inside of eutectic particles (Fig. 4 a)). As Fe was reported in nano-scaled TiB_2 for annealed amorphous Fe-Ti-B, these Fe-rich phases are not particularly caused by the uptake of N during nitriding [6]. If the precipitation of Fe inside particles was increased by the uptake of N or only depending on the inherent heat treatment could not be determined here. Matrix grains inside the diffusion zone displayed an abnormal morphology compared to the bulk material and indicated slightly higher hardness than the compound layer with increased N-content (Fig. 4 a)). Bright lines (orange circle in Fig. 4 a)) were mostly orientated perpendicular to the N-diffusion direction and presumably indicated deformations in the surface zone. If these deformation originated from residual stresses of the

thermochemical process or were induced by the expanded ferrite, which can result in plastic deformation and grain swelling [27–30], has to be further investigated. The dark areas predominantly around primary and clustered particles probably did not originate from delamination between the soft matrix and stiff particles, since in-situ formed TiB_2 generally results in a good cohesion between particles and matrix [31,32]. Polishing artefacts or interface debonding caused by the performed etching process are more likely to have caused these cracks. TiB_2 possess a higher electrochemical resistance than the surrounding matrix and the emerged topography after etching may locally enhanced the etching effect around primary and clustered particles.

Plasma nitriding of the Fe-Cr-B-C material resulted in a significant surface hardness increase (Fig. 1). Like for the nitrided Fe-Ti-B material, no Fe-nitrides could be detected and thereby the hardness enhancement probably also originated from expanded ferrite (Fig. 6). The accomplished surface hardness peak is comparable to a plasma nitrided X12Cr13 martensitic stainless steel [18,33]. During nitriding precipitation of Cr-nitrides was reported for austenitic [34–37], ferritic [38,39] and martensitic [18,40,41] stainless steels and is generally accelerated by nitriding temperatures >450 °C [20]. This threshold temperature was exceeded by the deployed 540 °C process temperature, but instead of forming nitrides existing particles undergo an apparently diffusion-controlled transformation of M_2B particles into CrN (Fig. 5). Fig. 7 displays an EDS line scan of a transformed particle, here for a prior M_2B of a Fe-6.0Cr-1.6B alloy plasma nitrided under the same conditions as Fe-Cr-B-C. In contrast to the M_2B particle, the CrN phase shows an oscillating concentration profile for Fe and Cr, which indicates a spinodal decomposition of CrN. Further investigations with higher resolution are required to describe the transformation process in detail. The particle transformation in the surface layer rendered in an overall particle hardness and E_r loss (Fig. 5 d)). M_2B particles compared to reported values yielded in roughly 100 GPa smaller E_r and higher hardness than calculated for Cr_2B [42]. Whereas the determined hardness of transformed CrN was similar to reported values [43]. Nevertheless, the particle transformation caused by the nitriding process had a detrimental effect on the hardness and Young's modulus of the newly formed CrN particles, which may have an influence on the performance under high pressure contact. Despite the individual hardness decrease of formed CrN, the overall surface hardness still increased after nitriding, which indicates that the hardness increase in the surface zone was governed by the expanded ferrite phase. The formation of CrN particle reduces the corrosion resistance of ferritic and martensitic stainless steels by local Cr-depletions in the matrix [18,26,33,44–46]. As only prior $(Fe,Cr)_2B$ seemed to transform and no additional CrN were formed, which generally decrease the matrix' Cr-content, it can be hypothesized that the Cr-depletion and corresponding loss in corrosion resistance should be less detrimental for nitrided Fe-Cr-B-C. Indicated cracks in the surface layer (arrows Fig. 5 b)) were predominantly inside or close to CrN and seem to emerge from residual M_2B inside the transformed particle. Whether the cracks originated from the inherent stresses of the expanded ferrite in the surface layer or the particle transforming process is still unclear. The additional zone between 50 and 80 µm, that was only detected in the OM micrograph (Fig. 1 b)), was probably accumulated with C, since N tends to push C in front of the nitriding layer [47].

5. Summary and conclusions

The effect of low-pressure carburizing and plasma nitriding on high modulus steels was investigated. Specific material/hardening technique combinations, namely carburizing of Fe-Ti-B and Fe-Cr-B as well as nitriding of Fe-Ti-B and Fe-Cr-B-C, were selected to gain first insights into the underlying hardening phenomena. The surface hardness was successfully enhanced, and nitriding resulted in an overall higher hardness (up to 1200 HV0.05) with a smaller surface layer compared to carburizing similar to conventional steels. Based on the performed mechanical and microstructural investigations, the following conclusions can be drawn:

- Carburizing of Fe-Ti-B did not result in the desired surface hardening due to excessive Ti-content. Carburizing Fe-Cr-B increased the surface hardness by forming a martensitic surface zone containing $M_{23}C_6$ carbides.
- The formation of expanded ferrite led to an increased surface hardness for nitrided Fe-Ti-B and Fe-Cr-B-C. Nitriding of Fe-Cr-B-C yielded in a diffusion-controlled particle transformation from M_2B to CrN, which had a detrimental effect on the particle's hardness and reduced Young's modulus.
- From the investigated alloys, Fe-Cr-B is preferred for carburizing while Fe-Cr-B-C with is preferred for nitriding, as its already hard martensitic matrix reduces spalling of the even harder nitride layer
- Power transmitting components strongly benefit from surface hardened high modulus steels, as their enhanced stiffness enables smaller tolerances at higher loads in the linear-elastic regime, reducing their inertia and thus decreasing energy consumption and enhancing performance.

6. Outlook

Future investigations of thermochemical treatment for high modulus steels can analyze further property improvements for specific material/hardening technique combinations or determine the thermal stability and performance of the hardened layers. A finer microstructure, for

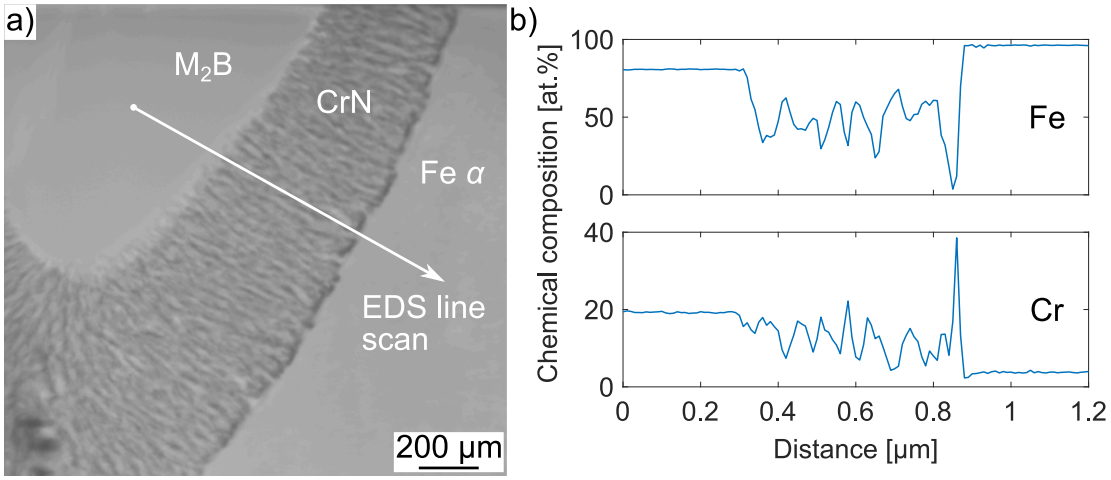

Fig. 7. Chemical analyses of a transformed CrN particle from plasma nitrided Fe-6Cr-1.6B (wt%) a) STEM image b) EDS line scan for selected elements.

example via additive manufacturing [51] or spray forming [52], could enhance the nitriding kinetics [53,54]. Spalling or cracking in the surface layer can be reduced by decreasing the hardness deviation of surface layer and base material, with matrix strengthening of Fe-Cr-B-C [12] and Fe-Cr-Ni-B alloys [55] by common steel heat treatments. Furthermore, sequentially carburizing and nitriding [21] or nitrocarburizing [50] can lead to a decreased hardness deviation between the surface layer and base material.

CRediT authorship contribution statement

M. Gathmann: Writing – review & editing, Writing – original draft, Visualization, Investigation, Formal analysis, Data curation. **N. Tönnißen:** Writing – original draft, Visualization, Investigation, Data curation. **C. Baron:** Writing – review & editing, Methodology, Investigation, Conceptualization. **A. Kostka:** Writing – review & editing, Visualization, Investigation, Data curation. **M. Steinbacher:** Writing – review & editing, Methodology. **H. Springer:** Writing – review & editing, Supervision, Project administration, Funding acquisition, Conceptualization.

Declaration of competing interest

The authors declare that they have no known competing financial interests or personal relationships that could have appeared to influence the work reported in this paper.

Data availability

Data will be made available on request.

Acknowledgement

D. Klapproth, F. Rütters and F. Schlüter are gratefully acknowledged for their support with synthesis and processing, as are M. Nellessen and T. Freieck for metallography and microscopy, Z. Meshou for hardness measurements and H. Bögershausen for nanoindentation. H. Springer, M. Gathmann and N. Tönnißen gratefully acknowledge financial support from the Heisenberg program of the Deutsche Forschungsgemeinschaft [DFG; project 416498847], German Federation of Industrial Research Associations [AiF; project 21460], and the Luftfahrtforschungsprogramm by the German Federal Ministry for Economic Affairs and Climate Action [BMWK LuFo; project 20T1913B].

References

[1] F. Bonnet, V. Daeschler, G. Petitgand, High modulus steels: new requirement of automotive market. How to take up challenge? Can. Metall. Quart. 53 (2014) 243–252, https://doi.org/10.1179/1879139514Y.0000000144.
[2] M.F. Ashby, D. Cebon, Materials selection in mechanical design, J. Phys. IV France 03 (1993), https://doi.org/10.1051/jp4:1993701. C7-1-C7-9.
[3] I.A. Ibrahim, F.A. Mohamed, E.J. Lavernia, Particulate reinforced metal matrix composites — a review, J. Mater. Sci. 26 (1991) 1137–1156, https://doi.org/10.1007/BF00544448.
[4] D.B. Miracle, Metal matrix composites – From science to technological significance, Compos. Sci. Technol. 65 (2005) 2526–2540, https://doi.org/10.1016/j.compscitech.2005.05.027.
[5] R.G. Munro, Material properties of titanium Diboride, J. Res. Natl. Inst. Stand. Technol. 105 (2000) 709–720, https://doi.org/10.6028/jres.105.057.
[6] H. Springer, R. Aparicio Fernandez, M.J. Duarte, A. Kostka, D. Raabe, Microstructure refinement for high modulus in-situ metal matrix composite steels via controlled solidification of the system Fe–TiB2, Acta Mater. 96 (2015) 47–56, https://doi.org/10.1016/j.actamat.2015.06.017.
[7] K. Tanaka, T. Saito, Phase equilibria in TiB2-reinforced high modulus steel, JPE 20 (1999) 207–214, https://doi.org/10.1361/105497199770335730.
[8] C. Baron, H. Springer, D. Raabe, Combinatorial screening of the microstructure–property relationships for Fe–B–X stiff, light, strong and ductile steels, Materials & Design 112 (2016) 131–139, https://doi.org/10.1016/j.matdes.2016.09.065.
[9] C. Baron, H. Springer, D. Raabe, Development of high modulus steels based on the Fe – Cr – B system, Mater. Sci. Eng. A 724 (2018) 142–147, https://doi.org/10.1016/j.msea.2018.03.082.
[10] G.R. Speich, A.J. Schwoeble, W.C. Leslie, Elastic constants of binary iron-base alloys, MT 3 (1972) 2031–2037, https://doi.org/10.1007/BF02643211.
[11] H. Zhang, H. Springer, R. Aparicio-Fernández, D. Raabe, Improving the mechanical properties of Fe – TiB2 high modulus steels through controlled solidification processes, Acta Mater. 118 (2016) 187–195, https://doi.org/10.1016/j.actamat.2016.07.056.
[12] C. Baron, H. Werner, H. Springer, On the effect of carbon content and tempering on mechanical properties and stiffness of martensitic Fe–18.8Cr–1.8B–xC high modulus steels, Mater. Sci. Eng. A 809 (2021) 141000, https://doi.org/10.1016/j.msea.2021.141000.
[13] G. Petzow, Metallographisches, keramographisches, plastographisches Ätzen, seventh. leicht korrigierte Auflage, Gebrüder Borntraeger, Stuttgart, 2015.
[14] M. Tarakci, K. Korkmaz, Y. Gencer, M. Usta, Plasma electrolytic surface carburizing and hardening of pure iron, Surf. Coat. Technol. 199 (2005) 205–212, https://doi.org/10.1016/j.surfcoat.2005.02.117.
[15] F. Çavuşlu, M. Usta, Kinetics and mechanical study of plasma electrolytic carburizing for pure iron, Appl. Surf. Sci. 257 (2011) 4014–4020, https://doi.org/10.1016/j.apsusc.2010.11.167.
[16] R. Aparicio-Fernández, H. Springer, A. Szczepaniak, H. Zhang, D. Raabe, In-situ metal matrix composite steels: effect of alloying and annealing on morphology, structure and mechanical properties of TiB2 particle containing high modulus steels, Acta Mater. 107 (2016) 38–48, https://doi.org/10.1016/j.actamat.2016.01.048.
[17] O.K. von Goldbeck, IRON—Binary Phase Diagrams, Springer Berlin Heidelberg, Berlin, Heidelberg, 1982.
[18] C.X. Li, T. Bell, A comparative study of low temperature plasma nitriding, carburising and nitrocarburising of AISI 410 martensitic stainless steel, Mater. Sci. Technol. 23 (2007) 355–361, https://doi.org/10.1179/174328407X161204.
[19] B. Wang, W. Fu, F. Dong, G. Jin, W. Feng, Z. Wang, S. Sun, Significant acceleration of nitriding kinetics in pure iron by pressurized gas treatment, Materials & Design 85 (2015) 91–96, https://doi.org/10.1016/j.matdes.2015.07.013.
[20] H. Berns, W. Theisen, Eisenwerkstoffe - Stahl und Gusseisen, fourth ed., Springer, Berlin Heidelberg, Berlin, Heidelberg, 2008.
[21] T. Christiansen, M.A.J. Somers, Low temperature gaseous nitriding and carburising of stainless steel, Surf. Eng. 21 (2005) 445–455, https://doi.org/10.1179/174329405X68597.
[22] A. Fossati, F. Borgioli, E. Galvanetto, T. Bacci, Glow-discharge nitriding of AISI 316L austenitic stainless steel: influence of treatment time, Surf. Coat. Technol. 200 (2006) 3511–3517, https://doi.org/10.1016/j.surfcoat.2004.10.122.
[23] S. Thaiwatthana, X.Y. Li, H. Dong, T. Bell, Comparison studies on properties of nitrogen and carbon S phase on low temperature plasma alloyed AISI 316 stainless steel, Surf. Eng. 18 (2002) 433–437, https://doi.org/10.1179/026708402225010083.
[24] B.C. Schibicheski Kurelo, G.B. de Souza, F.C. Serbena, C.M. Lepienski, P.C. Borges, Mechanical properties and corrosion resistance of αN-rich layers produced by PIII on a super ferritic stainless steel, Surf. Coat. Technol. 403 (2020) 126388, https://doi.org/10.1016/j.surfcoat.2020.126388.
[25] R.R.M. de Sousa, F.O. de Araújo, J.A.P. Da Costa, A.M. de Oliveira, M.S. Melo, C. Alves Junior, Cathodic cage nitriding of AISI 409 ferritic stainless steel with the addition of CH4, Mat. Res. 15 (2012) 260–265, https://doi.org/10.1590/S1516-14392012005000016.
[26] J. Alphonsa, S. Mukherjee, V.S. Raja, Study of plasma nitriding and nitrocarburising of AISI 430F stainless steel for high hardness and corrosion resistance, Corros. Eng. Sci. Technol. 53 (2018) 51–58, https://doi.org/10.1080/1478422X.2017.1396648.
[27] S. Grigull, S. Parascandola, Ion-nitriding induced plastic deformation in austenitic stainless steel, J. Appl. Phys. 88 (2000) 6925–6927, https://doi.org/10.1063/1.1321019.
[28] J.C. Stinville, C. Templier, P. Villechaise, L. Pichon, Swelling of 316L austenitic stainless steel induced by plasma nitriding, J. Mater. Sci. 46 (2011) 5503–5511, https://doi.org/10.1007/s10853-011-5494-8.
[29] J.C. Stinville, P. Villechaise, C. Templier, J.P. Riviere, M. Drouet, Plasma nitriding of 316L austenitic stainless steel: experimental investigation of fatigue life and surface evolution, Surf. Coat. Technol. 204 (2010) 1947–1951, https://doi.org/10.1016/j.surfcoat.2009.09.052.
[30] J.C. Stinville, P. Villechaise, C. Templier, J.P. Rivière, M. Drouet, Lattice rotation induced by plasma nitriding in a 316L polycrystalline stainless steel, Acta Mater. 58 (2010) 2814–2821, https://doi.org/10.1016/j.actamat.2010.01.002.
[31] Z. Hadjem-Hamouche, J.-P. Chevalier, Y. Cui, F. Bonnet, Deformation behavior and damage evaluation in a new titanium Diboride (TiB2) steel-based composite, Steel Research Int. 83 (2012) 538–545, https://doi.org/10.1002/srin.201100255.
[32] S. Lartigue-Korinek, M. Walls, N. Haneche, L. Cha, L. Mazerolles, F. Bonnet, Interfaces and defects in a successfully hot-rolled steel-based composite Fe–TiB 2, Acta Mater. 98 (2015) 297–305, https://doi.org/10.1016/j.actamat.2015.07.024.
[33] P. Corengia, G. Ybarra, C. Moina, A. Cabo, E. Broitman, Microstructure and corrosion behaviour of DC-pulsed plasma nitrided AISI 410 martensitic stainless steel, Surf. Coat. Technol. 187 (2004) 63–69, https://doi.org/10.1016/j.surfcoat.2004.01.031.
[34] G.A. Collins, R. Hutchings, K.T. Short, J. Tendys, X. Li, M. Samandi, Nitriding of austenitic stainless steel by plasma immersion ion implantation, Surf. Coat. Technol. 74-75 (1995) 417–424, https://doi.org/10.1016/0257-8972(95)08370-7.
[35] W. Liang, Surface modification of AISI 304 austenitic stainless steel by plasma nitriding, Appl. Surf. Sci. 211 (2003) 308–314, https://doi.org/10.1016/S0169-4332(03)00260-5.

[36] F. Borgioli, A. Fossati, E. Galvanetto, T. Bacci, Glow-discharge nitriding of AISI 316L austenitic stainless steel: influence of treatment temperature, Surf. Coat. Technol. 200 (2005) 2474–2480, https://doi.org/10.1016/j.surfcoat.2004.07.110.
[37] B.-Y. Jeong, M.-H. Kim, Effects of pulse frequency and temperature on the nitride layer and surface characteristics of plasma nitrided stainless steel, Surf. Coat. Technol. 137 (2001) 249–254, https://doi.org/10.1016/S0257-8972(00)01095-1.
[38] T. Bacci, F. Borgioli, E. Galvanetto, G. Pradelli, Glow-discharge nitriding of sintered stainless steels, Surf. Coat. Technol. 139 (2001) 251–256, https://doi.org/10.1016/S0257-8972(01)01010-6.
[39] B. Larisch, U. Brusky, H.-J. Spies, Plasma nitriding of stainless steels at low temperatures, Surf. Coat. Technol. 116-119 (1999) 205–211, https://doi.org/10.1016/S0257-8972(99)00084-5.
[40] H. Dong, M. Esfandiari, X.Y. Li, On the microstructure and phase identification of plasma nitrided 17-4PH precipitation hardening stainless steel, Surf. Coat. Technol. 202 (2008) 2969–2975, https://doi.org/10.1016/j.surfcoat.2007.10.036.
[41] C.E. Pinedo, W.A. Monteiro, On the kinetics of plasma nitriding a martensitic stainless steel type AISI 420, Surf. Coat. Technol. 179 (2004) 119–123, https://doi.org/10.1016/S0257-8972(03)00853-3.
[42] M.-M. Zhong, C. Huang, C.-L. Tian, The structural stabilities, mechanical properties and hardness of chromium tetraboride: compared with low-B borides, Int. J. Mod. Phys. B 30 (2016) 1650201, https://doi.org/10.1142/S0217979216502015.
[43] C. Baron, H. Springer, Properties of particle phases for metal-matrix-composite design, Data Brief 12 (2017) 692–708, https://doi.org/10.1016/j.dib.2017.04.038.
[44] E. de Araújo, R.M. Bandeira, M.D. Manfrinato, J.A. Moreto, R. Borges, S.D.S. Vales, P.A. Suzuki, L.S. Rossino, Effect of ionic plasma nitriding process on the corrosion and micro-abrasive wear behavior of AISI 316L austenitic and AISI 470 super-ferritic stainless steels, J. Mater. Res. Technol. 8 (2019) 2180–2191, https://doi.org/10.1016/j.jmrt.2019.02.006.
[45] C.A. Figueroa, F. Alvarez, D.R.G. Mitchell, G.A. Collins, K.T. Short, Previous heat treatment inducing different plasma nitriding behaviors in martensitic stainless steels, J. Vac. Sci. Technol. A 24 (2006) 1795–1801, https://doi.org/10.1116/1.2219759.
[46] H.-J. Spies, C. Eckstein, H. Zimdars, Structure and corrosion behaviour of stainless steels after plasma and gas nitriding, Surf. Eng. 18 (2002) 459–460, https://doi.org/10.1179/026708402225006286.
[47] M. Tsujikawa, N. Yamauchi, N. Ueda, T. Sone, Y. Hirose, Behavior of carbon in low temperature plasma nitriding layer of austenitic stainless steel, Surf. Coat. Technol. 193 (2005) 309–313, https://doi.org/10.1016/j.surfcoat.2004.08.179.
[50] H.-J. Spies, T. Bell, Z. Kolozsvary, Thermochemische Randschichtbehandlung nichtrostender Stähle bei tiefen Temperaturen, HTM Journal of Heat Treatment and Materials 65 (2010) 11–21, https://doi.org/10.3139/105.110044.
[51] H. Springer, C. Baron, F. Mostaghimi, J. Poveleit, L. Mädler, V. Uhlenwinkel, Additive manufacturing of high modulus steels: new possibilities for lightweight design, Addit. Manuf. 32 (2020) 101033, https://doi.org/10.1016/j.addma.2019.101033.
[52] H. Springer, C. Baron, A. Szczepaniak, V. Uhlenwinkel, D. Raabe, Stiff, light, strong and ductile: nano-structured high Modulus steel, Sci. Rep. 7 (2017) 2757, https://doi.org/10.1038/s41598-017-02861-3.
[53] J. Liu, S. Suslov, A. Vellore, Z. Ren, A. Amanov, Y.-S. Pyun, A. Martini, Y. Dong, C. Ye, Surface nanocrystallization by ultrasonic nano-crystal surface modification and its effect on gas nitriding of Ti6Al4V alloy, Mater. Sci. Eng. A 736 (2018) 335–343, https://doi.org/10.1016/j.msea.2018.08.089.
[54] W.P. Tong, N.R. Tao, Z.B. Wang, J. Lu, K. Lu, Nitriding iron at lower temperatures, Science 299 (2003) 686–688, https://doi.org/10.1126/science.1080216.
[55] C. Baron, H. Springer, On the effect of Ni additions to Fe – Cr – B high modulus steels, Mater. Des. 167 (2019) 107624, https://doi.org/10.1016/j.matdes.2019.107624.